Adaptive Lighting for Curved and Non-Uniform Objects in Opto-Mechanical Inspection Systems

Mark Gerges and Xu Chen[†]

Abstract—**Visual inspection is omnipresent and critical in precision manufacturing. However, complex geometries of parts hinder uniform illumination, and high reflectivity challenges accurate focusing for digital visual data collection. This research provides a novel adaptive illuminance distribution for consistent lighting to facilitate quality imaging over complex-shaped, highly reflective surfaces. The central approach entails using arrays of independently controlled light sources to reliably generate different lighting patterns, structures, and colors. Such results consider the geometry, the 3D pose of parts in the environment, and the surface topography of the work-piece to be inspected, hence amplifying the capabilities of an image capturing system. This paper discusses the mathematical problem formulation, the analytic solution, the optimality of the proposed lighting, and experimental results in imaging curved parts common in aerospace manufacturing. The efficacy of the resulting defect identification is tested using a deep neural network.**

Keywords: Robotic Imaging, Controlled Lighting, Optimal Lighting, Illuminance Distribution, Glare and Gradient Elimination, Machine Learning.

I. INTRODUCTION

Omnipresent in manufacturing and especially within aerospace, visual inspection is a prime target for innovations in automation for manufacturing. Modern precision manufacturing must exclude parts with imperfections such as scratches, discolorations, dents, and tool marks. When air flows into a jet engine at 1.2 tons per second during takeoff, defects as minor as scratches and pits in the turbine blades could lead to imbalances in airflow and part fatigue, resulting in premature engine wear and even engine failures [1]–[3]. Not only is inspecting such complex shiny surfaces tiring and time-consuming, but the inspection process is also burdensome, subjective, and requires months to years of training. As a result, automated inspection has become essential for gas turbine production [4], [5].

At the core of automating precision visual inspection is the proper data collection and controlled-environment imaging to profile a 3-dimensional object under inspection. A good image is the result of the most suitable focus and illumination of the desired surface. However, complex geometries of parts hinder uniform illumination, and high reflectivity challenges accurate focusing (Fig. 1). Setting up a proper controlled environment is thus key and potentially a transformative way to amplify

contrast and sharpness for quality imaging [6], leading to reliable and repeatable data collection for precision inspection.

This paper proposes a novel adaptive illuminance distribution for quality visual imaging and robotic inspections of complex reflective parts. Small tolerance for errors renders standard machine vision unreliable to inspect defects at millimeter to micrometer scales. Directed lighting has proven to benefit image formation but is limited to incrementally inspecting sections of a curved surface [7]. Leveraging arrays of independently controllable light sources spatially arranged over the part under inspection, however, the proposed optomechatronics allow for the generation of different lighting patterns, structures, and colors to cover a large surface area. From there, we formulate a convex optimization, particularly a constrained least-squares problem, that integrates (1) the geometry and 3D pose of parts in the environment, and (2) the surface topography of the work-piece to be inspected. In particular, we propose five solutions of adaptive lighting and benchmark each physical configuration. Images are captured under the implemented lighting, and imaging data sets are collected for a group of curved parts with characteristics common in gas turbine industry. The efficacy of the methods is compared under a machine-learning based defect identification with transfer learning. The results appeared key in perfecting the performance of the neural network. A visual-centric workflow is also immediately interpretable for humans, and traceable to other process steps from machining to polishing, leading to cost-effective implementation and quality assurance in the production of entire engines and aircraft.

Fig. 1: Example complex metallic parts in precision manufacturing.

The contributions of the paper are threefold. First, we provide a new method of controlled illumination with multiple spatially arranged light sources for precision visual inspection of complex reflective surfaces. Second, we elucidate an automation workflow integrating controlled environment data collection with machine learning to achieve a first-instance defect detection at over 95% accuracy for a class of critical aerospace metallic parts. Third, through extensive benchmarking, the paper provides untapped insights to light objects challenging to image even for experienced human inspectors. More broadly, a diverse range of industries have benefited from recent advances in machine vision technologies: e.g., general manufacturing, robotic guidance, part identification, visual

inspection, process control, characterization, fault detection, and inventory management [8]–[14]. Examples of industry-specific applications include aerial refueling [15], disease/-contamination identification, and leaf recognition [16]–[18]. Improvements resulting from this research have the potential to empower machine vision to increase quality control standards in these important problem spaces, by eliminating glare and lighting gradients, and emphasizing surface defects and deviations over non-uniform and uneven topographies.

The remainder of this paper is organized as follows. Section II discusses the different reflectivity of surfaces and lighting structures. Section III presents a preliminary understanding of lighting physics and illustrates an experimental proof of concept, establishing a strategy for uneven topographies. Section IV delivers the proposed adaptive lighting and experimentally validates the defect identification. Section V extends the optimal solution by considering the effect of scaling the numbers of light sources and lighting angles. Section VI concludes the paper and provides directions of future work.

II. BACKGROUND AND LIGHTING SELECTION

Automating the visual inspection process requires the employment of an optomechatronic system. Such a system must capture images of a work-piece and then analyze the resulting pixel-domain data, rather than analyzing the physical work-piece itself. Therefore, it is critical to understand how the light will reflect off the surface to be inspected. Factors that characterize the reflected lights include the work-piece material, its topography and surface characteristics such as finish and color, the light source itself, and environmental conditions [6], [19]. Below, we summarize the relevant physics for inspection and along the process, provide the proposed hardware component designs.

A. Reflectivity of Surfaces

Flat surfaces are uniform and easily illuminated, whereas curved, uneven surfaces challenge illumination, and prismatic surfaces have sharp edges and/or steep slopes that are difficult to illuminate due to shadows and glints [6], [20]. In addition to geometry, inspection must also consider surface finish of the parts. Specular and highly polished surfaces cause the light to be reflected at an angle equal and opposite to the angle of incidence. Diffuse surfaces are rough and dull, causing the incident light to be scattered in many directions. Directional surfaces, on the other end, have fine and uniform grooves that reflect light in a preferred direction dependent on the angle of incidence. All three types of surfaces are encountered in precision inspection, and are considered in our selection of the light source and lighting structure in Section II-C.

B. Lighting Structure and Source

Interference and disturbances such as sunlight and excessive room lighting substantially impact the quality and consistency of inspection. High-power strobing can overwhelm the wash out the ambient contribution, but is expensive and ergonomically challenging. Additionally, not all light sources (e.g.,
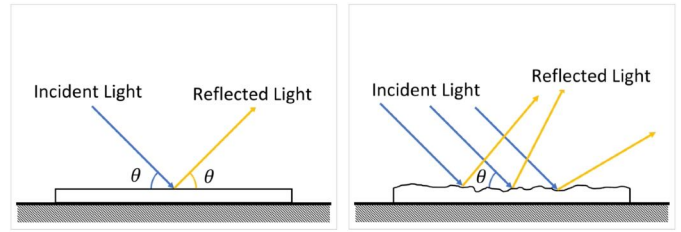
Fig. 2: Surface reflection: (a) specular (b) diffuse

fluorescent lights) are capable of strobing. Another solution entails using a physical enclosure to block environmental lighting – a method that applies most suitably to small objects. In both cases, the lighting must be controlled to maintain a consistent luminosity.

The structure, location, and pattern of lighting also impact the efficacy of a machine vision system. There are two parent structures for placing light sources with respect to the work-piece, source, and image capture system. The first is front illumination, where the light source and the receiver are on the same side of the part. The second is back illumination.

Front illumination applies direct or angled ring lights with the image capture system at the center of the light source, leading to shadow-less illuminations. Sharper angles of incidence on the surface lead to better detection of edges, scratches, and embossing. Diffuse, flat, and coned ring lights are suitable for inspecting specular surfaces with minimum glinting and shadows. Dome lights use a dome-shaped concentrator to direct the light beams and are used for curved and specular surfaces (Fig. 3 top left). However, they require close proximity to the part, making it difficult for complex geometries. Co-axial lights apply a 2-way mirror to direct light at an angle of 90° onto the work-piece. These lights are used for specular surfaces and often also require close proximity to the part (Fig. 3 top right). The last two types of relevant front lighting are dark and bright-field illumination. When trying to achieve a dark focused region, and the surfaces being inspected are uneven, dark-field lighting is most advisable to illuminate bright defects. When the focus is on bright areas and flat surfaces, bright-field lighting is most advisable [21].

For back illumination, two instances are shown in Fig. 4. Dimensional analysis, hole inspection, and checking for the absence of components are the core benefits here [22].

C. Proposed Lighting Shape and Source Selection

From Sections II-A and II-B, front and flat/dome diffuse lighting rise as the most suitable options for uneven topographies and surface finishes. In this study, we select front and flat diffuse lighting as the baseline illumination for inspecting the targeted metallic objects.

After the pattern and lighting methodology, we move onto the selection of the light source. For the targeted robotic inspection, fluorescent lights produce diffuse lighting that is cool and white, and provides a large illumination area at low cost. However, they suffer from inflexible fixed shapes, short lifetimes, significant temperature drift, rapid aging, and
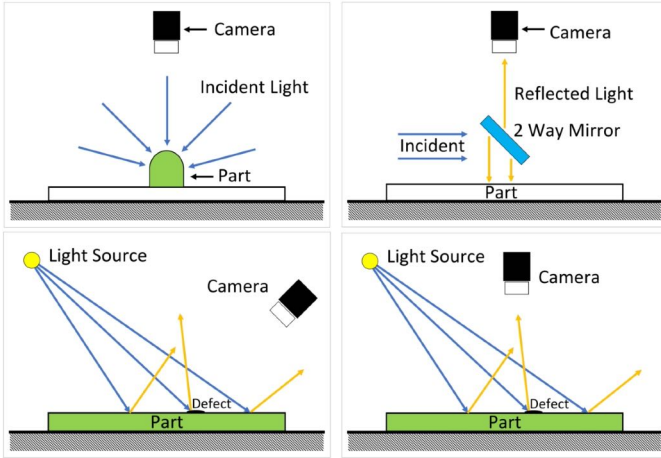
Fig. 3: Front illumination: top left to bottom right: dome, co-axial, bright-field and dark-field illumination.
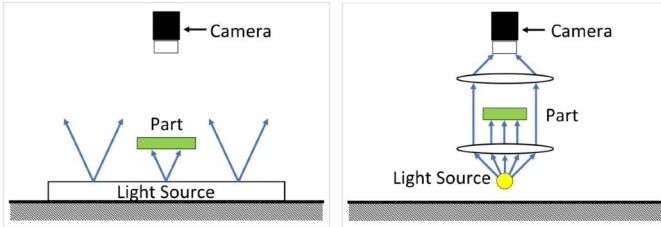

Fig. 4: Back illumination: back and collimated configurations.

long switching transients. Also, if Pulse Width Modulation (PWM) is used to control the brightness, a high frequency (22 kHz or more) ballast is required to reduce flicker interference [21], [22]. Halogen lights provide high intensity and broad-spectrum lighting, but suffer from a short lifetime and a significant brightness drop near the end of the service life. They also produce a large amount of heat, exhibit long switching transients, and require robust stabilization. Light-emitting diodes (LEDs) provide pulse and strobe capable monochromatic light. They have long lifetimes and small temperature drifts, produce relatively low heat, and are stable, consistent, and cost-effective. Xenon lights provide pulse and strobe capability, and monochromatic light capable of high-color temperatures (5,500 to 12,000 K). On the downside, they require high voltages and more expensive electronics than LEDs to control. They also age faster than LEDs. Metal halide (Mercury/High-Pressure Sodium) lights are used in large-scale applications or when requiring very bright light sources. Still, they suffer from high (e.g., 30 KV) working voltages, are expensive, and produce substantial heat.

Table I summarizes the relative strength of different lighting under performance criteria relevant to inspecting complex metallic parts [19]–[21]. For the focused precision inspection, based on the allowable work distance, intensity, stability and on-time, we selected different weighting for each property. As shown, the most suitable light source for complex reflective parts are LEDs to supply flat diffuse lighting. We implemented

such a lighting source in the work-space by using a 120 LED shooting tent with a diffuser. This arrangement will be utilized moving forward, and an additional set of auxiliary (compensatory) LED lights will be employed in Section III-A.

TABLE I: Proposed lighting selection criteria.

Property (/5)	Wts.	LED	Halogen	Fluorescent	Xenon
Life Exp.	0.1	5	1.5	3	3.5
App. Flexibility	0	4.5	3	2	2.5
Output Stability	0.20	5	1.5	3	2.5
Cost Eff./hr	0	4	2.5	3.5	2.5
Strobing	0	5	1	0	4
On time	0.20	5	5	5	5
Output Int.	0.1	4	4	3	5
Heat Output	0	4	1	3.5	3
Reaction Time	0	5	1	1	5
Robustness	0.1	5	1	3	1
Maintenance	0.1	5	1	3	4
Safety	0.1	5	3	4	1
Area/Distance	0.1	3	4	5	4
Score	1.00	4.70	2.75	3.70	3.35

III. PROPOSED LIGHTING CONTROL

This section summarizes the mathematical problem of lighting curved surfaces, explains the lighting physics, and develops the proposed strategy for uneven topographies.

A. Light Physics and the Proposed Geometric Lighting Model

Light can be measured through different techniques, resulting in different representations and metrics. Luminous Intensity (measured in Candela, or in short, cd) represents the amount of light emitted in the range of a three-dimensional angular span. This is a property of the light source available from the data-sheets. Since the angular span is constant regardless of the source's distance, the luminous intensity is equal for surfaces A and B in Fig. 5a.
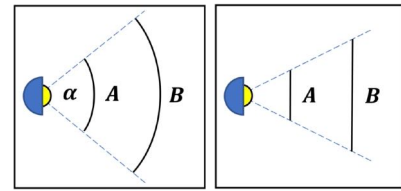

Fig. 5: (a) Lighting in angular span: A and B have the same luminous intensity (b) Lighting on surface: illuminance of A larger than that of B.

If the luminous intensity is not included in the data-sheet, the aforementioned angular span, measured in steradians and denoted as Ω, is used to calculate the luminous intensity. Similar to radians, steradians are unit-less, and 1 steradian in a sphere of 1-meter radius would produce a surface area of $1\ m^2$, which indicates that the sphere would have 4π steradians. This angle is calculated using the apex angle of the light source, denoted as α, through:

$$\Omega = 2\pi(1 - \cos(\alpha/2)) \tag{1}$$

One can then calculate the luminous intensity by [23], [24]:

$$I = L/\Omega \qquad (2)$$

where I is the luminous intensity, and L is the luminous flux (in lumen) that measures the perceived power of light.
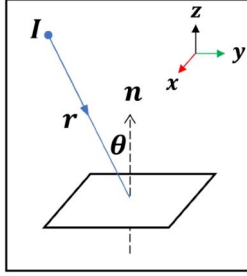

Fig. 6: Relationship between luminous intensity and illuminance.

The final critical property is illuminance, measured in Lux and represents the illumination of a surface as opposed to that of an angle. This measurement is the easiest to compare to, since it is affected by the angle of incidence of the light (θ) and the distance between the source and surface (r) (Fig. 6). The more distant the surface is from the source, or the larger the angle of incidence, the less the illumination will be. In Fig. 5b, for example, surface A has greater illuminance values than that of B. We calculate illuminance at a single point on a surface by [23], [24]:

$$E = \frac{I \cos(\theta)}{r^2} \qquad (3)$$

To calculate the illuminance at a point on a surface from the proposed multi-source lighting, we generalize Eq. (3) to

$$E = \sum_{i=1}^{n} \frac{I_i \cos(\theta_i)}{r_i^2} \qquad (4)$$

where n is the number of light sources, and I_i, θ_i and r_i are the luminous intensity, angle of incidence, and distance of each light source, respectively (Fig. 6). The proposed lighting with LEDs implements a WS2812B [25] 8×8 light array integrated with a control circuit and RGB chip, allowing each unit to provide independently controlled brightness and color.

TABLE II: WS2812B data-sheet luminous intensity.

Emitting Color	Model	Wavelength (nm)	Luminous Intensity (mcd)	Voltage (V)
Red	13CBAUP	620 - 630	550 - 700	1.8 - 2.2
Green	13CGAUP	515 - 530	1100 - 1400	3.0 - 3.2
Blue	10RIMUX	465 - 475	200 - 400	3.0 - 3.4

Since a white LED can consist of three smaller red green and blue (RGB) diodes, each source has its luminous intensity range as shown in Table II. For the focused while-light illumination, to avoid using a spectrometer to identify the contribution of each color, we created a performance correction factor, C_l, that normalizes the weighted luminous intensity by:

$$I_i = C_l(R_{\max} + G_{\max} + B_{\max}) = C_l(0.7 + 1.4 + 0.4) = 2.5C_l$$

where C_l and the maximum luminous intensity contribution of each color ($R_{\max} = 0.7cd$, $G_{\max} = 1.4cd$ and $B_{\max} = 0.4cd$) are used to approximate the 8×8 light source's final capabilities. We derived the performance correction factor by installing the lights at a measured elevation above a work-surface and comparing the calculated illuminance E_c using Eq. (4) with the measured illuminance (E_a) at a given point. The performance correction factor is then calculated via:

$$C_l = \frac{E_a}{E_c}$$

Further generalizing the equation to cover any point in the work-space when multiple lights are used, we introduce the notation $(i|j)$ to represent the relative position of the light sources (i) to the point being studied (j). Then

$$E_j = \sum_{i=1}^{n} \frac{I_i \cos(\theta_{(i|j)})}{r_{(i|j)}^2}$$

Putting the above into a vector and matrix form yields our geometric model of multi-source lighting:

$$\begin{bmatrix} E_1 \\ \vdots \\ E_m \end{bmatrix} = \begin{bmatrix} \frac{\cos(\theta_{(1|1)})}{r_{(1|1)}^2} & \cdots & \frac{\cos(\theta_{(1|n)})}{r_{(1|n)}^2} \\ \vdots & \ddots & \vdots \\ \frac{\cos(\theta_{(m|1)})}{r_{(m|1)}^2} & \cdots & \frac{\cos(\theta_{(m|n)})}{r_{(m|n)}^2} \end{bmatrix} \begin{bmatrix} I_1 \\ \vdots \\ I_n \end{bmatrix} \qquad (5)$$

where m represents the number of points on the desired surface and n is the number of light sources being controlled.

B. *Proposed Optimization-based Illuminance Distribution*

Denoting Eq. (5) as $E = AI$ and noting that m is usually much larger than n, we can solve for the luminous intensity vector I with the method of least-squares:

$$I \approx (A^T A)^{-1} A^T E$$

However, since the luminous intensity of any physical light is bounded between 0 and a maximum value $I_{\max}$, we propose a box constrained least-squares and solve a convex optimization problem:

$$I = \arg\min_{I} \frac{1}{2} \|AI - E\|_2^2 \qquad (6)$$

$$\text{subject to: } 0 \leq I_i \leq I_{\max}, \ i = 1, 2, \ldots, n \qquad (7)$$

The optimization can be readily solved through the interior-point method. Such a formulation enables taking an illuminance distribution as the input to produce the luminous intensity and structure of the different light sources required to supply the desired distribution. To illustrate the solution's validity we developed a model system in a smaller work-space (Fig. 7). The controllable lights were fixed at a leveled height off of a flat surface, and the coordinates of the lights in relation to a local coordinate system were recorded. This

process was executed in the absence of ambient lights to avoid external disturbances and emphasize the validity of the proposed optimization-based solution.
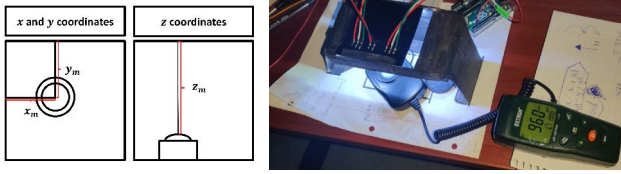

Fig. 7: Prototype flat-surface inspection and experimental setup (meter measuring 1,000 Lux).

Using the optimal solutions, we imposed two illuminance distributions for performance validation: a constant 1,000 Lux and a constant 5,000 Lux over the full surface in the physical setup. The calculated luminous intensities and structure of the light source were input into the lighting controller (Fig. 8 column 1), and the illuminance of the surface was measured at random points for performance comparison (point 1 to point 8 in Fig. 8 column 2).
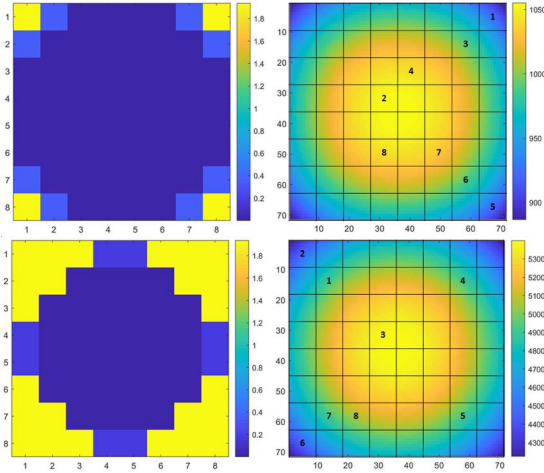
Fig. 8: Proposed optimal solution: top - 1,000 Lux [(a) intensity (b) illuminance]; bottom - 5,000 Lux [(c) intensity (d) illuminance].

Fig. 7 shows the experimental setup where the 1,000 Lux solution was imposed, where the meter reads an actual value of 960 Lux. Table III shows the performance of the proposed solution under two different target illuminance values. As can be observed, for a target illuminance of 1,000 Lux, the actual illuminance lies in a close range of 878 - 963 Lux with a small 7.9% mean error and a 3% standard deviation. For a 5,000 Lux target illuminance, the proposed solution generates an effective actual lighting distribution in the range of 4,620 - 5,040 Lux with a 3.4% mean error and a 3% standard deviation.

C. Extension to Uneven Topographies

This section extends the proposed optimal lighting to a three-dimensional object. Accommodating three-dimensional surfaces requires the extraction of the pose and geometry of the work-piece. Since the work-piece is suspended in the work-space and has an uneven topography, it is challenging

TABLE III: Measured illuminance verifying design in Fig. 8.

Point	1,000 Lux	5,000 Lux
1	878	4,930
2	963	4,620
3	914	5,040
4	961	4,960
5	887	4,800
6	906	4,680
7	916	4,720
8	941	4,980
Min.	878	4,620
Max.	963	5,040
Mean	921	4,841
Std. Dev.	30	147
Mean err.	79	169

to accurately measure lighting in the physical work-space. Simulations were executed to give further insight into the behavior of illuminance over curved surfaces. Specifically, we use Autodesk Revit to model a work-space of a $0.5m \times 0.5m \times 0.5m$ shooting tent with 120 base LEDs fixed at the top with a diffuser (Fig. 9).
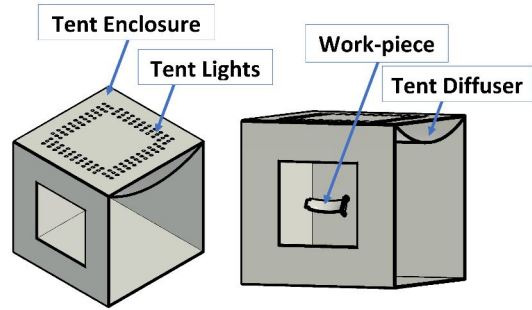

Fig. 9: Design of work-space in Autodesk Revit.

1) Simulation Verification: We first verified the proposed high-fidelity simulation in Revit by benchmarking the physics-based calculations in the previous section. In Fig. 10, the solution for the 1,000 Lux distribution on a flat surface is imposed from Fig. 8 inside the recreated work-space. The results of the simulation are compared with the experimentally measured results (Table IV). We observe only minor deviations from the physics based calculation (mean error: 3.6%, std: 6.7%), verifying the capabilities of Revit to produce accurate illuminance distributions.
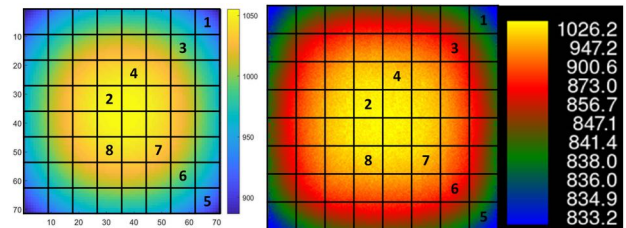

Fig. 10: Solution of 1,000 Lux illuminance distribution: (a) Physics-based calculation (b) Revit high-fidelity simulation.

TABLE IV: Experimental verification of simulation in Fig. 10.

Point	Measured	Simulated
1	878	838
2	963	1,026
3	914	873
4	961	986
5	887	838
6	906	873
7	916	924
8	941	966
Min.	878	838
Max.	963	1,026
Avg.	921	916
Std. Dev.	30	67
Mean err.	79	36

2) Simulation Insight: With the successful verification of the proposed simulation setup, we expose the work-piece to different scenarios to extract useful insights. Fig. 11 shows the illuminance distribution over the work-piece in Revit compared to an actual captured image from the physical system. There is a clear correlation between the simulated illuminance distribution and the glare in the physically captured images. We measure glare using the Unified Glare Rating, or UGR, for Discomfort Glare [26], [27] and through contrast (Disability Glare) [28]:

$$\text{UGR} = 8\log_{10}\left[\frac{0.25}{L_b}\sum_{i=1}^{n}\left(\frac{L_i^2\omega_i}{p_i^2}\right)\right]$$

$$\text{Contrast} = \frac{L_{max} - L_{min}}{L_{max} + L_{min}}$$

where L_i is the luminous flux of a luminaire, ω_i is the solid angle of the luminaire as seen by the viewer, p_i is the Guth position index measuring the angular distance from the center of the viewer's line of sight to the luminaire, and L_b is the luminous flux of the background. In both cases, there is a ratio between different levels of luminous flux. As illustrated in Section III-A, the luminous intensity I is directly proportional to the luminous flux L with a factor of $1/\Omega$ [Eq. (2)]. This in turn is proportional to the illuminance E using Eq. (4).
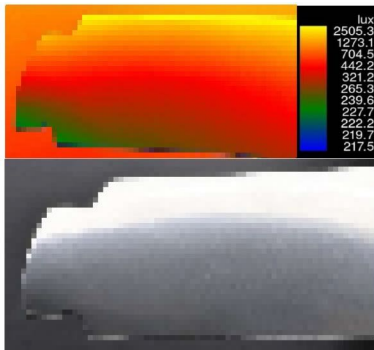

Fig. 11: Glare/gradient comparison: (1) Revit simulation, (2) captured images (pixelated and distorted for compliance policies).

Furthermore, different defect sizes and orientations were implemented on the work-piece with varying widths x and depths y (Fig. 12 and Table V) to visualize the interaction between the illuminance distribution and defect orientation. When the defect is perpendicular to the illuminance gradient, visibility of the defect increases with the defect size. Whereas in the parallel orientation, visibility of the defect remains at the same level across different defect sizes. Maintaining a consistent illuminance distribution over the surface will eliminate the dependence of defect orientation with respect to the gradient by increasing the contrast between lighting on the surface and within the defect. Therefore, from Fig. 11 and Table V, it is clear that enforcing a consistent illuminance distribution on the inspection surface is key to eliminating glare and light gradients.
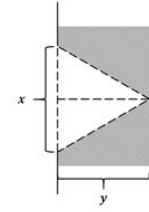

Fig. 12: Design of experiments: engineered defect shape.

TABLE V: Modelled defect sizes (µm).

X (µm)	Y (µm)	Parallel	Perpendicular
50	250		
10	50		
5	2.5		

3) Proposed Shape-Adaptive Lighting for Curved Parts: When a curved part is subject to an existing illuminance ($[E]_E$) and we have a desired illuminance over the work-piece surface ($[E]_D$), we calculate a compensatory illuminance ($[E]_C$) to balance the uneven existing distribution (Fig. 13). At the core of the multi-source lighting, we have the superposition:

$$\begin{bmatrix} E_1 \\ \vdots \\ E_m \end{bmatrix}_D = \begin{bmatrix} E_1 \\ \vdots \\ E_m \end{bmatrix}_C + \begin{bmatrix} E_1 \\ \vdots \\ E_m \end{bmatrix}_E$$

which yields the target compensation from the assistive lights:

$$\begin{bmatrix} E_1 \\ \vdots \\ E_m \end{bmatrix}_C = \begin{bmatrix} E_1 \\ \vdots \\ E_m \end{bmatrix}_D - \begin{bmatrix} E_1 \\ \vdots \\ E_m \end{bmatrix}_E$$
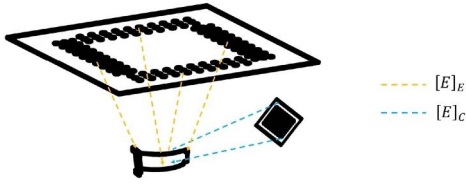
Fig. 13: Outline of proposed lighting hardware configuration.

For the proposed LED array system, we have:

$$
\begin{bmatrix} E_1 \\ \vdots \\ E_m \end{bmatrix}_C = \begin{bmatrix} \frac{\cos(\theta_{(1|1)})}{r^2_{(1|1)}} & \cdots & \frac{\cos(\theta_{(1|n)})}{r^2_{(1|n)}} \\ \vdots & \ddots & \vdots \\ \frac{\cos(\theta_{(m|1)})}{r^2_{(m|1)}} & \cdots & \frac{\cos(\theta_{(m|n)})}{r^2_{(m|n)}} \end{bmatrix} \begin{bmatrix} I_1 \\ \vdots \\ I_n \end{bmatrix}
$$

Solutions of luminous intensity I can then be solved from the aforementioned model-based optimization in Section III-B.

As highlighted earlier, the work-space has 120 base LEDs which represent $[E]_E$. Fig. 14 shows the work-space, the 15 proposed positions for the work-piece to be inspected, the line of sight of the camera, and the 120 LEDs. Since the work-piece is a 3D surface, the angle between the incident light and the surface normal is used as an indicator of inclusion in the calculation through conditioning the term $\cos(\theta_{i|j})$, to avoid any negative contributions when the light ray enters from the back of the point of interest, i.e. when $\cos(\theta_{(i|j)}) < 0$ we assign $\cos(\theta_{(i|j)}) = 0$.
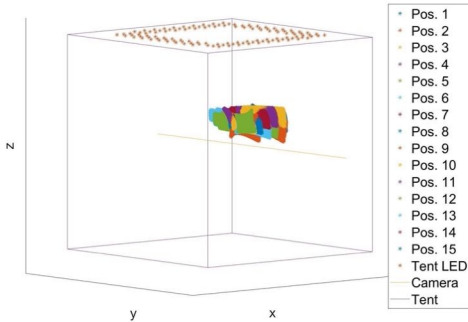

Fig. 14: Work-space and work-piece placement.

For a well-rounded comparison, six different configurations (C_0 - C_5) were considered for $[E]_D$:

- Case C_0: Lighting in the shooting tent was tuned as best as possible with diffused LED lighting at the ceiling of Fig. 14. No compensatory lighting is applied, i.e., $[E]_D = [E]_E$.
- Case C_1: Setting the maximum value of $[E]_E$ as $[E]_D$, namely, we aim for uniform illuminance at the maximum environment condition: $[E]_D = \max[E]_E$.
- Case C_2: Setting the maximum value of $[E]_E$ in a 1/8 sub-region ($E(s)$) as $[E]_D$ and focus in this sub-region only: $[E]_{D(s)} = \max[E]_{E(s)}$ and $[E]_{D(\neq s)} = 0$.
- Case C_3: Setting the maximum value of $[E]_E$ in a sub-region (1/8) as $[E]_D$ and leave other regions unconstrained: $[E]_D = \max[E]_{E(s)}$.

- Case C_4: Setting the maximum value of $[E]_E$ in a sub-region (1/16) as $[E]_D$ and focus in this sub-region only: $[E]_{D(s)} = \max[E]_{E(s)}$ and $[E]_{D(\neq s)} = 0$.
- Case C_5: Setting the maximum value of $[E]_E$ in a sub-region (1/16) as $[E]_D$: $[E]_D = \max[E]_{E(s)}$.

Using the chosen $[E]_D$, we calculated the additional LED mesh contribution $[E]_C$. Then using the proposed boxed least-squares, the required luminous intensity $[I]$ was calculated. An example of the optimal solution was calculated for configuration C_1 in the work-piece's first position below. The existing illuminance distribution $[E]_E$ was calculated over the surface (Fig. 15b), following which the desired illuminance $[E]_D$ and the needed compensatory illuminance $[E]_C$ were derived (Fig. 16a). Fig. 16b presents the resulting optimal luminous intensity and structure of the LED arrays. Fig. 17 shows the corresponding generated illuminance distribution and the final illuminance of the work-piece. For this work, 15 solutions were derived, one for each work-piece position. These were programmed into the LED controller to produce the optimal lighting shape for each position.
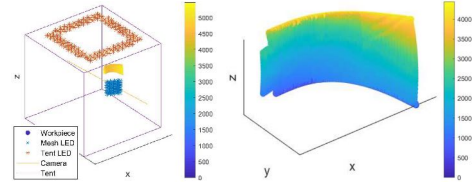

Fig. 15: Validation of proposed adaptive illuminance on a demo part: (a) work-space arrangement, (b) existing illuminance $[E]_E$. (Dimensions of the demo part do not scale.)
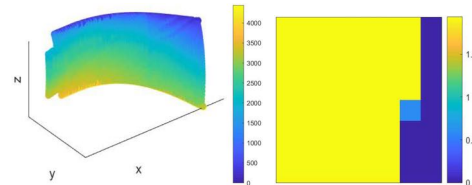

Fig. 16: Validation of proposed adaptive illuminance on a demo part: (a) compensatory illuminance $[E]_C$, (b) least-squares luminous intensity $[I]$.
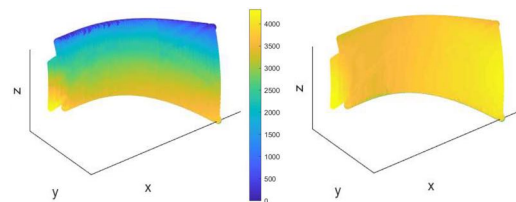

Fig. 17: Validation of proposed adaptive illuminance on a demo part: (a) actual compensation, (b) final calculated illuminance.

IV. RESULTS AND COMPARISONS

Comparing Figs. 15b, and 17b, we observe that indeed the final distribution of illuminance over the surface is significantly improved. Table VI compares all the focal areas on

the sample curved geometry under different lighting configurations. We calculated the means, standard deviations, and absolute mean errors of the final illuminance values for all 15 positions within the proposed arrangements. Figs. 18, 19 and 20 compare the performances of C_0 and C_1, C_2 and C_3, and C_4 and C_5 respectively with respect to the desired $[E]_D$. A summary of the average standard deviations and errors are shown in Table VII.

TABLE VI: Adaptive lighting comparison. Positions 1 and 15 have been distorted for date release compliance.

Pos.	C_0	C_1	C_2	C_4	C_5
1					
2					
3					
4					
5					
6					
7					
8					
9					
10					
11					
12					
13					
14					
15					

TABLE VII: Average standard deviations and mean absolute errors.

Quantity	C_0	C_1	C_2	C_3	C_4	C_5
Std. Dev.	1,235	1,277	1,081	1,245	1,240	1,283
Mean Err.	2,837	950	2,023	944	2,366	1,308

All the proposed optimal solutions successfully compen-
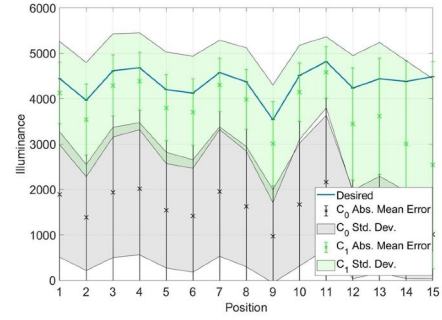

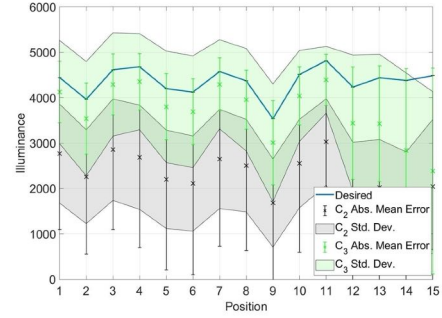Fig. 18: Mean, standard deviation and error of C_0 and C_1.

Fig. 19: Mean, standard deviation and error of C_2 and C_3.

sated for the baseline lighting, exhibiting errors lower than that of C_0, with C_1 and C_3 having mean errors less than 1,000 Lux. Fig. 21 compares the performance of C_1 and C_3, highlighting the similarity in the achieved illuminance.

With the improved image data, the efficacy testing of the optimal solutions was assessed by examining the ease and accuracy of defect identification on images of aerospace curved metallic parts captured using the adaptive lighting. Using 854 images of defective parts and 581 images of good parts, the defect identification is achieved through a Resnet 50 deep neural network under transfer learning, with the following properties: images size for input: 448 pixels by 448 pixels; training epochs (number of complete passes through the training data-set): 20; learning rate: 0.0001; data augmentation: scale (0.9~1), flip-x, flip-y. The training data include the images captured of the work-piece under lighting configurations C_0 - C_5, together with another set of common images captured at varying lighting conditions at a 3 : 7 ratio. Five neural networks were subsequently trained, one for each lighting configuration (due to the similarity in performance shown in Fig. 21, C_3 was omitted from this analysis). Table VIII highlights the final defect detection performance. As can be seen, compared to the C_0 baseline, training and validation accuracy is improved all around. C_1 and C_2 improve the performance of the defect identification further than C_4 and C_5. A reduction in false alarms and miss rates is also achieved. Table. VI compares C_0 to C_5 (excluding C_3) for all positions of the work-piece in front of the camera, where the cropped regions represent the focal areas of the image capture system.
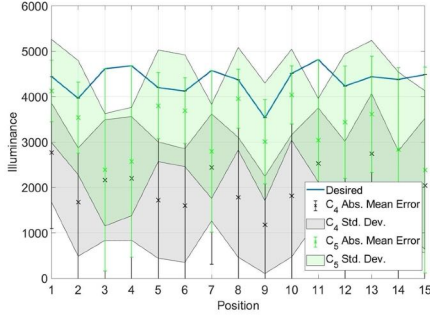
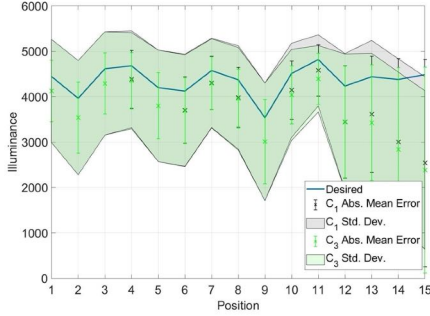Fig. 20: Mean, standard deviation and error of C_4 and C_5.

Fig. 21: Mean, standard deviation and error of C_1 and C_3.

The compensation is clearly visible with reduced gradients and glare. Overall, C_2 outperforms other solutions with the highest training and validation accuracy, and lowest false alarm and miss rates. However, the margin over C_1 is sufficiently small statistically that C_1 and C_2 are on the same performance level.

TABLE VIII: Results of proposed defect identification.

Light	Valid. %	Train. %	False Alarm %	Miss Rate %
C_0	94.00 ±0.63	96.52	4.29 ±1.13	7.71 ±1.25
C_1	95.51 ±0.46	97.67	3.35 ±0.98	5.62 ±0.96
C_2	95.63 ±0.35	98.28	3.29 ±0.12	5.46 ±0.58
C_4	94.19 ±0.13	97.73	3.85 ±0.70	7.77 ±0.10
C_5	94.70 ±0.50	98.15	3.81 ±1.06	6.79 ±1.35

V. EXTENSION AND THE EFFECT OF SCALING

Using the results obtained for a fixed array of light sources (64 LEDs), we extended the proposed method to cases with a larger number of lights at different lighting angles to reveal the effect of scaling and resolution. For example, consider two additional forms with increased numbers of lighting angles: 1) Four 8×8 LED arrays, surrounding the camera (256 LEDs emitting from four flat surfaces), and 2) A single dome array with the same spacing as the 8×8 LED array (252 LEDs emitting from a curved surface). The structures considered have the same granularity, but with a greater number of sources at different angles. A representation in the work-space and a sample of their boxed least-squares solutions are outlined in Figs. 22 and 23.
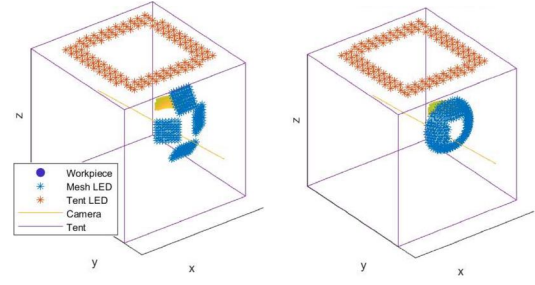

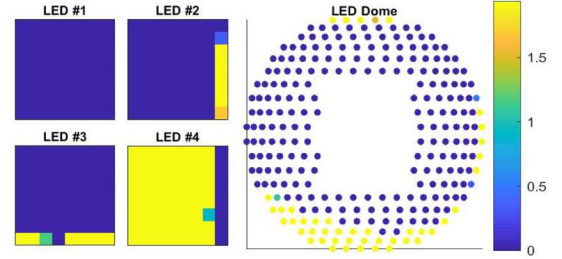Fig. 22: Light structures: (a) four 8×8 arrays (b) dome array.

Fig. 23: Optimal solutions: (a) four 8×8 arrays (b) dome array.

Fig. 24 and Table IX compare the standard deviations and absolute mean errors of both arrangements. We observe an approximate reduction by a factor of two in standard deviations and errors due to the increased number of light sources and lighting angles of attack. This increase in coverage allows the compensatory lights to have a view of the whole surface. This is further highlighted in Fig. 25 and Table X, which illustrate the results of one position of the work-piece under C_0, C_1, and the two extended structures of lighting.
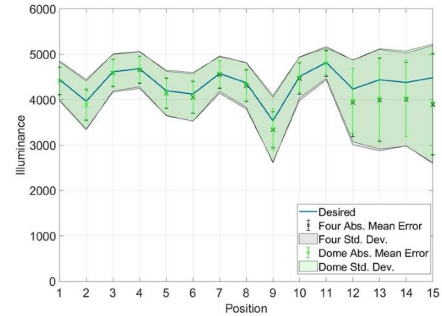

Fig. 24: Performance of extended multi-source illumination.

TABLE IX: Performance gains across 15 positions.

Quantity	C_0	C_1	Four	Dome
Std. Dev.	1,235	1,277	642	638
Mean Err.	2,837	950	479	483

VI. CONCLUSIONS AND FUTURE WORK

This study has presented a novel adaptive lighting methodology for curved reflective surfaces, along with five design
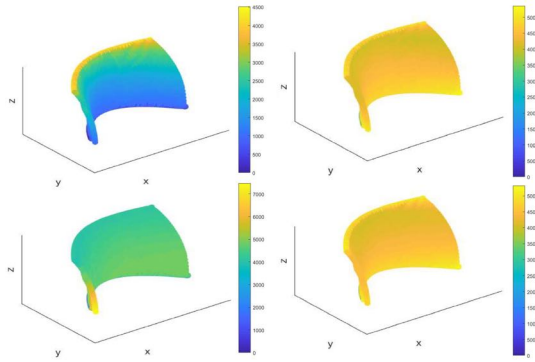
Fig. 25: Final illuminance distribution: (top left) C_0 (bottom left) C_1 (top right) four 8×8 arrays (bottom right) dome array.

TABLE X: Average stds and mean absolute errors of C_0, C_1, four array and dome array arrangements for position 10.

Configuration	C_0	C_1	Four Panel	Dome
Std. Dev.	1,353	1,036	480	450
Mean Err.	2,844	644	347	338

configurations, and two extensions to the lighting structure. The results appeared key in perfecting the neural network learning performance: using less than 1500 raw images, the proposed lighting yielded over 95% identification accuracy with less than a 5% false-alarm rate. In particular, at a nearly saturated benchmark, the shape-adaptive lighting increased training (+1.8%) and validation (+1.6%) accuracies, and reduced false alarms (-1.0%) and miss rates (-2.25%). This was achieved while using 70% of the training data with no adaptive lighting, and 30% using the proposed solutions.

All proposed adaptive solutions provide performance gains over a well-tuned shooting tent configuration C_0. The quantitative comparison of standard deviations and errors of the five solutions showed C_1 and C_3 having the best distributions, closely resembling the desired illuminance level. C_1 and C_2 exhibited the best defect identification performance, with C_2 slightly outperforming C_1. The result is understandable in that for machine learning, a more localized approach (C_2) following the focus of the image capture system helps to maintain the desired illuminance in the region of interest. Such an effect is demonstrated in Fig. 26, which shows a section of a captured work-piece outside the focal area under the arrangements of lighting.
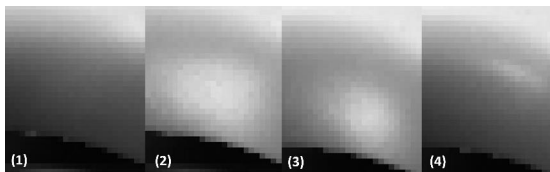

Fig. 26: Sample resulting images: (1) C_0 (2) C_1/C_3 (3) C_2 (4) C_4/C_5 (pixelated and distorted for data release compliance).

Though the optimal lighting solution was capable of eliminating glare and gradient within the focal region (Table VI), we have not considered the direct reflection of the light sources in the work-piece. Direct reflection occurs when the angle of incidence on the work-piece from the sources is equal and co-planar with the angle of reflection into the camera. Therefore, despite the optimal solutions of C_1 and C_3 being numerically superior to C_2, C_4 and C_5, the positioning of the work-piece can cause the light sources to be directly reflected into the camera, leading to glinting in images. As a result, the higher-intensity solutions (C_1, C_2 and C_3) can exhibit noise that interferes with the defect identification. Furthermore, C_4 and C_5 are far more constrained than the remaining solutions due to the large number of sub-regions, causing limited compensation and improvements over the baseline. This is reflected in the quantitative analysis (Fig. 20), the defect identification result (Table VIII), as well as Fig. 26.1 and Fig. 26.4.

With the extension in Section V, the optimal solutions are further enhanced significantly by a twofold improvement in standard deviation and mean error (Figs. 24 and 25, and Tables IX and X). The extensions apply an increased number of lights and lighting angles, with the same light-source granularity (10mm spacing) and luminous intensity capabilities. Studying the standard deviation and error plots of all proposed solutions and extensions with changing positioning of the work-piece indicated a performance drop in the last four positions (Figs. 18, 19, 20 and 24). Here, the focus of the camera is on the convex side of the work-piece in positions 12 - 15, which creates a challenge in lighting the full surface due to the reduced view factor between each light source and the full surface. We can address this geometric constraint and the direct light reflection by incorporating adaptive positioning to the lighting, to increase the mobility and adaptability of the inter-spatial relationship between the work-piece, the camera, and the lighting. This would help eliminate blinding effects in the captured images and further cancel glare and gradient. Furthermore, a lower granularity and increased luminous intensity would enhance the performance.

Including obstacles in the computing formulation would allow for more elaborate and intricate lighting structures and work-spaces, increasing the adaptability of the calculation. Another future improvement would be the inclusion of Lambertian reflections to account for all lighting in the work-space that reflects off all surfaces. This would reduce the need for correction factors. Finally, employing a spectrometer to measure all the exact spectral response of the lights would improve the analytical solution and alleviate the dependence on correction factors.

REFERENCES

[1] A. Hamed and W. Tabakoff, "Erosion, Corrosion and Foreign Object Damage Effects in Gas Turbines," *AGARD Conference Proceeding 558*, vol. 1994, no. November, p. Paper No.11, 1994.

[2] P. Brauny, M. Hammerschmidt, and M. Malik, "Repair of air–cooled turbine vanes of high–performance aircraft engines – problems and experience," *Materials Science and Technology*, vol. 1, no. 9, pp. 719–727, 1985.

[3] J. Renshaw, S. D. Holland, R. B. Thompson, and D. J. Eisenmann, "Synthetic defects for vibrothermography," *AIP Conference Proceedings*, vol. 1211, pp. 498–504, 2010.

[4] J. Aust and D. Pons, "Comparative Analysis of Human Operators and Advanced Technologies in the Visual Inspection of Aero Engine Blades," *Applied Sciences (Switzerland)*, vol. 12, no. 4, 2022.

[5] B. Sampson, "Introduction to non-destructive testing," Aerospace Testing International, Accessed Mar. 02, 2021. [Online]. Available: https://www.aerospacetestinginternational.com/features/introduction-to-non-destructive-testing.html

[6] S. Anand and L. Priya. 52 Vanderbilt Avenue, New York, NY 10017: CRC Press Taylor Francis Group, 2019.

[7] M. Dalla Valle, P. Gallina, and A. Gasparetto, "Mirror synthesis in a mechatronic system for superficial defect detection," *IEEE/ASME Transactions on Mechatronics*, vol. 8, no. 3, pp. 309–317, 2003.

[8] H. Golnabi and A. Asadpour, "Design and application of industrial machine vision systems," *Robotics and Computer-Integrated Manufacturing*, vol. 23, no. 6, pp. 630–637, 2007.

[9] W. J. Pastorius, "Machine vision for industrial inspection metrology and guidance," in *Fourth Annual Canadian Conference Proceedings., Programmable Control and Automation Technology Conference and Exhibition*, 1988, pp. 13A2–1/1.

[10] Z. Liu, H. Ukida, P. Ramuhalli, and D. S. Forsyth, "Integrated imaging and vision techniques for industrial inspection: A special issue on machine vision and applications," *Machine Vision and Applications*, vol. 21, no. 5, pp. 597–599, 2010.

[11] R. French, M. Benakis, and H. Marin-Reyes, "Intelligent sensing for robotic re-manufacturing in aerospace - An industry 4.0 design based prototype," *Proceedings - 2017 IEEE 5th International Symposium on Robotics and Intelligent Sensors, IRIS 2017*, vol. 2018-Janua, pp. 272–277, 2018.

[12] Q. Zhou, R. Chen, B. Huang, C. Liu, J. Yu, and X. Yu, "An automatic surface defect inspection system for automobiles using machine vision methods," *Sensors (Switzerland)*, vol. 19, no. 3, 2019.

[13] Y. L. Kaan K. Katircioglu, "Machine vision technology for shelf inventory," U.S. Patent 0 262 116 A1, Mar. 02, 2021. [Online]. Available: https://patents.google.com/patent/US20150262116A1/en

[14] N. I. Giannoccaro, A. Massaro, L. Spedicato, and A. Lay-Ekuakille, "Detection analysis of small notches damages using a new tactile optical device," *IEEE/ASME Transactions on Mechatronics*, vol. 20, no. 1, pp. 313–320, Feb 2015.

[15] G. Campa, M. R. Napolitano, and M. L. Fravolini, "Simulation environment for machine vision based aerial refueling for UAVs," *IEEE Transactions on Aerospace and Electronic Systems*, vol. 45, no. 1, pp. 138–151, 2009.

[16] Y. R. Chen, K. Chao, and M. S. Kim, "Machine vision technology for agricultural applications," *Computers and Electronics in Agriculture*, vol. 36, no. 2-3, pp. 173–191, 2002.

[17] R. W. Conners, D. E. Kline, P. A. Araman, and T. H. Drayer, "Machine vision technology for the forest products Industry," *Computer*, vol. 30, no. 7, pp. 43–48, 1997.

[18] V. Satti, A. Satya, and S. Sharma, "An Automatic Leaf Recognition System For Plant Identification Using Machine Vision Technology," *International Journal of Engineering Science and Technology (IJEST)*, vol. 4, no. 5, pp. 874–879, 2013.

[19] D. Martin, "A Practical Guide to Machine Vision Lighting - Part II," *Machine Vision Fundamentals*, pp. 7–9, 2013.

[20] N. Instruments, "A practical guide to machine vision lighting," NI, Accessed Mar. 02, 2021. [Online]. Available: https://www.ni.com/en-us/innovations/white-papers/12/a-practical-guide-to-machine-vision-lighting.html

[21] A. Hornberg, *Handbook of Machine Vision*. Weinheim, Germany: WILEY-VCH Verlag GmbH Co KGaA, 2006.

[22] D. Martin, "Basic Lighting Techniques for Machine Vision," *AIA Vision Conference*, pp. 1–68, 2016.

[23] A. E. F. Taylor, "Illumination Fundamentals," The Lighting Research Center, Troy, NY 12180, Tech. Rep., 2000.

[24] M. Phar, W. Jakob, and G. Humphreys, "Physically based rendering: From theory to implementation," Accessed Mar. 02 2021 [Online], 2021. [Online]. Available: https://www.pbr-book.org/3ed-2018/contents

[25] Worldsemi Co. LTD., *WS2812B LED Intelligent control integrated light source*, 2016. [Online]. Available: https://voltiq.ru/datasheets/WS2812B_datasheet_EN.pdf

[26] *Discomfort Glare In Interior Lighting CIE*, vol. 117-1995. International Commission on Illumination, 1995.

[27] H. Cai and T. Chung, "Evaluating discomfort glare from non-uniform electric light sources," *Lighting Research and Technology*, vol. 45, no. 3, pp. 267–294, 2013.

[28] T. M. Aslam, D. Haider, and I. J. Murray, "Principles of disability glare measurement: An ophthalmological perspective," *Acta Ophthalmologica Scandinavica*, vol. 85, no. 4, pp. 354–360, 2007.

Mark Gerges is a master student in the Department of Mechanical Engineering at the University of Washington (UW), Seattle. He received his bachelor's degree from The American University in Cairo (AUC), Egypt in 2013. His research focuses on vision-based inspection and robotics.

Xu Chen is an associate professor in the Department of Mechanical Engineering at the University of Washington (UW), Seattle. He received his M.S. and Ph.D. degrees in Mechanical Engineering from the University of California, Berkeley in 2010 and 2013, respectively, and his bachelor's degree with honors from Tsinghua University, China in 2008. His research focuses on dynamic systems, information processing, and controls, with applications to robotics and advanced manufacturing. He is a recipient of the U.S. National Science Foundation CAREER Award, the SME Sandra L. Bouckley Outstanding Young Manufacturing Engineer Award, and the Young Investigator Award from ISCIE / ASME International Symposium on Flexible Automation.